Measuring the magnetic anisotropy of the spin Hall effect and spin relaxation length in nickel and permalloy via electrical spin injection

Eoin Dolan [1,2] Jone Mencos [1,2] Williams Savero Torres [3] Maxen Cosset-Chéneau [4] Jean-Philippe Attané,[3] Laurent Vila [3] Luis E. Hueso [1,5] and Fèlix Casanova [1,5,*]

[1] *CIC nanoGUNE BRTA, 20018 Donostia-San Sebastian, Basque Country, Spain*

[2] *Departamento de Polímeros y Materiales Avanzados: Física, Química y Tecnología, University of the Basque Country (UPV/EHU), 20018 Donostia-San Sebastian, Basque Country, Spain*

[3] *University Grenoble Alpes, CEA, CNRS, Grenoble INP, SPINTEC, 38000 Grenoble, France*

[4] *Zernike Institute for Advanced Materials, University of Groningen, 9747 AG Groningen, The Netherlands*

[5] *IKERBASQUE, Basque Foundation for Science, 48009 Bilbao, Basque Country, Spain*

(Received 11 May 2025; revised 5 September 2025; accepted 9 September 2025; published 2 October 2025)

The spin Hall effect in ferromagnets is of great interest in the field of spintronics, and while the effect has been quantified in many materials, the dependence of the spin Hall angle on the relative orientation of spin polarization and the magnetization is less well studied. Of equal importance for the purpose of spin-charge interconversion in ferromagnets is the spin relaxation length, which is predicted to be highly anisotropic with respect to magnetization. Using a modified lateral spin valve geometry with a copper channel and permalloy spin injector, we measure the dependence of the spin Hall angle and spin relaxation length on magnetization orientation in permalloy and nickel, using two distinct device geometries. This allows us to disentangle the contributions of the spin relaxation length and spin Hall angle to the measured spin-charge interconversion voltage output. Our results indicate a large anisotropy in both the spin relaxation length and spin Hall angle in both permalloy and nickel, in agreement with theoretical calculations. The quantities change in opposite directions, with the spin relaxation length rising as the magnetization is moved parallel to the spin polarization and the spin Hall angle falling, leading to a near total cancellation of the spin-charge interconversion output.

DOI: 10.1103/dx73-2lp6

I. INTRODUCTION

The spin Hall effect (SHE) allows for the conversion of charge current into spin current and vice versa and is therefore of fundamental importance in the field of spintronics [1]. In typical spintronic devices, nonmagnetic heavy metals are used where components with strong SHE are required, with ferromagnets (FMs) being reserved for memory elements such as in magnetic random-access memory (MRAM) [2,3], and spin-based logic [4–6]. However, FMs can display SHE [7–11], with spin-charge interconversion (SCI) efficiencies comparable to heavy metals [11], and with the potential advantage of using their magnetization as an additional degree of freedom for control for SCI [11,12].

The spin Hall conductivity is expected to be anisotropic in FMs due to lowering of symmetry by the magnetization [13,14]. This is sometimes referred to as the spin anomalous Hall effect (SAHE), although we discuss the effect in terms of anisotropy in the SHE [15,16]. Where the SAHE is mentioned we are referring to literature sources which use this term [13,17]. A spin current in a FM is expected to produce a charge current which depends on the relative orientation of the spin with the magnetization, which defines the direction of spin polarization in a FM at equilibrium. It has been speculated that the SHE and AHE can be related to one another by the FM polarization [18] but, in practice, the relationship between the SHE and AHE in a FM is quite complex [13], and thus the SHE should be considered in terms of the spin Hall conductivity [10,13,14].

The anisotropy of the SHE has been studied in several different FMs, such as CoFeB [8,19], FePt [20], CoFe [21], NiFe (permalloy, Py) [7,22–25], Co [26], CoTb [27], NiCu [11,28,29], NiPd [11], and Fe [30] using a variety of measurement techniques. Results are mixed with some studies showing the SHE to be isotropic [11,26,28,29] and others showing it to be anisotropic [8,19–24,27,30]–whether this is due to experimental differences or material dependent is yet to be established. Theoretical studies of Ni predict a large difference in the SHE with magnetization [13,16,31], which should be easily resolvable in our experiment. In Py, prior experimental work [22,23] has shown an appreciable anisotropy. However prior works on this topic do not typically consider a dynamic spin relaxation length (λ_s) which is also expected to vary greatly with magnetization orientation in both Py and Ni [32], meaning the effects of λ_s and the spin Hall angle (θ_{SHE}) are entangled.

In this work, we study the SHE in Py and Ni, using lateral spin valves (LSVs) in a nonlocal configuration to produce a pure spin current. Note that we measure the inverse SHE, but the direct SHE can be obtained by swapping the current and voltage terminals, which follows Onsager reciprocity [33,34].

*Contact author: f.casanova@nanogune.eu

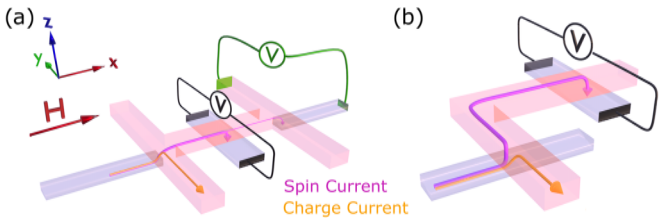

FIG. 1. Device schematic. Two geometries were used in this work to measure the SHE. (a) H-shaped device, consisting of two Py elements (gray) along $\hat{x}$, referred to as the injector (left) and detector (right), with a third perpendicular element (absorber, center) along $\hat{y}$ made of either Py or Ni, all connected by the Cu channel (orange). Two voltage measurements are indicated: in black is the SHE configuration (corresponding to results in Fig. 3), and in green the spin absorption configuration (corresponding to results in Fig. 2). (b) L-shaped device, again showing a Py injector (along $\hat{x}$), and a Py or Ni absorber (along $\hat{y}$) with an associated spin Hall voltage (corresponding to results in Fig. 4).

For the sake of simplicity, we refer to both as the SHE. This method of spin injection and detection provides for a clear and unambiguous analysis of the results [7]. This geometry allows us to clearly separate the spin injecting and detecting FMs, reducing the chances of spurious effects from spin injection and eliminating the chance of exchange interaction between the FMs. We employ a geometry which allows us to measure the anisotropy of θ_{SHE} with magnetization by independently controlling the magnetization of the spin injecting and detecting FMs, while simultaneously accounting for the anisotropy of λ_s in the FM. In this way, we observe a large anisotropy of both θ_{SHE} and λ_s, depending on the relative orientation of the spin polarization of the FM magnetization. Crucially, with the spin polarized perpendicular (parallel) to the magnetization, we see a minimum (maximum) in λ_s and a maximum (minimum) in θ_{SHE}, with the product of the two, and therefore the measured voltage due to SHE, being approximately constant.

II. DEVICE

We study Py and Ni, prototypical FM examples, which both form a high-quality transparent interface with the Cu we use for our spin channel. Our measurements indicate that the interface resistance between the two materials is in fact limited by the Sharvin resistance, which forms a key part of our analysis [35,36]. Py is used as the spin injecting material in all devices, since Ni cannot be used to inject or detect spin current in LSVs, with it having zero current spin polarization [37,38].

Our FMs are deposited by electron-beam deposition onto a clean Si/SiO_x substrate using standard lithographic techniques. All FM elements are 30 nm thick and 140 nm wide, with lengths of $\approx$2 μm. The spin injector and detector have different switching fields due to engineered shape anisotropies (the addition of a nucleation pad far from the Cu/Py junction favors magnetic domain-wall formation, lowering the switching field). After depositing the FM elements, the lithography defining the Cu channel, either H-shaped, Fig. 1(a), or L-shaped, Fig. 1(b), was performed. Before Cu deposition, the interfaces of the FMs were cleaned using Ar-ion milling to ensure a transparent and Ohmic interface, and a Cu channel (140 nm wide and 90 nm thick) was deposited by thermal evaporation in ultrahigh vacuum. All lateral dimensions were confirmed by scanning electron microscopy (SEM), and thicknesses were confirmed by x-ray diffraction (XRD). The SHE element of the devices (henceforth referred to as the absorber), indicated with the black voltage probe in Figs. 1(a) and 1(b) is either Py or Ni, with both materials studied in the same geometries.

TABLE I. Key material properties extracted from reference measurements and simulations at 10 K.

Material	$\lambda_s^{\parallel}$ (nm)	ρ (Ω nm)	α
Py	2.6 ± 0.2	313 ± 5	0.33 ± 0.02
Cu	1350 ± 50	19 ± 2	0

First, we characterized our material properties, including bulk resistivities ρ, which were obtained using four-point electrical measurements combined with device dimensions from SEM imaging. We calculated the interface resistances between Cu/Py and Cu/Ni [39], although this was found to be smaller than our experimental resolution and, in fact, the intrinsic Sharvin resistance is likely the dominant interface term (see Note S3 of the Supplemental Material [40]). The saturation magnetic fields for Py and Ni were found via anisotropic magnetoresistance (AMR) measurements (see Note S4 [40]). We also measured, using a separate reference device with a conventional LSV geometry, the spin relaxation length for a spin current polarization oriented parallel to the magnetization ($\lambda_s^{\parallel}$) in Py, as well as the spin polarization of Py (α_{Py}), which are shown in Table I (see Notes S1 and S2 for details [40]). These were extracted using three-dimensional (3D) FEM simulations with GETDP [41] and GMSH [42], of LSVs with different channel lengths, together with data from an LSV with an absorbing Py element [43,44]. This is particularly important because Py will be used to inject spin in both the H-shaped and L-shaped devices, with the injector always oriented parallel to the magnetic field, so we can use the values derived from the reference device in the Py elements aligned with the magnetic field.

III. SPIN-ABSORPTION ANISOTROPY

The aim of this section is to quantify the spin relaxation anisotropy by measuring the spin-absorption anisotropy. To do this we employ an LSV configuration in the H-shaped device both with [Fig. 1(a), green circuit] and without an absorber. This is distinct from the analysis we do to extract $\lambda_s^{\parallel}$ in Py (Table I) as shown in Note S2 [40], because now the absorber is no longer magnetized in a direction parallel or antiparallel to the injector and detector, except at very high field. The absorber will still absorb spin, reducing the spin accumulation at the detector, but this absorption now depends on the applied magnetic field, which rotates the absorber magnetization from being perpendicular to the injector and detector at zero field to being parallel at high field. The absorption has been shown to be much more efficient in the perpendicular orientation [32] because the spins entering the absorber precess and dephase in the exchange field of the absorber. This results in a smaller

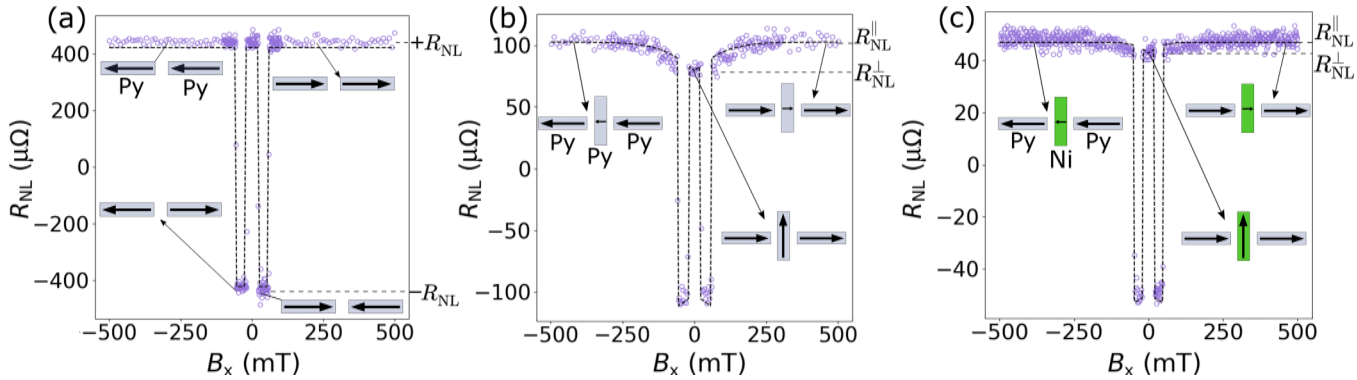

FIG. 2. Spin absorption anisotropy measurements using the H-shaped device, with a channel width of 130 nm and an injector-detector distance of 500 nm. (a) A reference LSV measurement, made in a device identical to that in Fig. 1(a) but without the central FM absorber. The relative orientations of the FM injector and detector magnetizations are indicated, corresponding to two measured nonlocal resistances, $\pm R_{NL}$, for parallel and antiparallel magnetizations. (b), (c) LSV measurements with an absorbing (b) Py and (c) Ni element placed between the injector and detector. The signal at high field is indicated as $R_{NL}^{\parallel}$ (spins polarized parallel to the absorber magnetization), and at zero field as $R_{NL}^{\perp}$ (spins polarized perpendicular to the absorber magnetization). The black dashed line represents a fit from a 3D FEM simulation.

signal at low field, where absorption is more efficient and little spin reaches the detector.

The results, showing the nonlocal resistance $R_{NL} = V_{NL}/I_c$, where V_{NL} and I_c are the measured nonlocal voltages and applied charge currents [green circuit, Fig. 1(a)], are plotted in Figs. 2(b) and 2(c). They demonstrate strong spin current absorption in both Py and Ni compared with the reference device [Fig. 2(a)]. At zero applied magnetic field (perpendicular configuration), Py absorbs $84 \pm 1\%$ and Ni absorbs $92 \pm 1\%$ of the spin current. In the parallel configuration, the absorption decreases to $78 \pm 1\%$ for Py and $89 \pm 1\%$ for Ni.

In the 3D FEM model, this is simulated by a changing value of the spin relaxation length, with λ_s being much shorter for spins oriented perpendicular to the magnetization. This value is denoted $\lambda_s^{\perp}$, where we expect $\lambda_s^{\parallel} > \lambda_s^{\perp}$. $\lambda_s^{\parallel}$ in Ni is extracted from the H-shaped device. Given that we know the value of $\lambda_s^{\parallel}$ in Py as well as α_{Py}, we can use these in the 3D FEM simulation for the Py injector and detector and vary $\lambda_s^{\parallel}$ in Ni until we match the high-field experimental R_{NL} signal in Fig. 2(c).

To find the value of $\lambda_s^{\perp}$ we employ the same approach but now focusing on R_{NL} at low field. We can keep the same value of $\lambda_s^{\parallel}$ for the injector and detector as we found from the reference device. Indeed, at high field we can also use these values for the absorber, which gives a good fit to the data at high field [Fig. 2(b)], although it deviates slightly in the H-shaped reference device [no absorber, Fig. 2(a)]. To fit the signal at low field, we vary $\lambda_s^{\perp}$ until we match the experimental R_{NL}. For the fitting curves shown in Figs. 2(b) and 2(c), for Py and Ni, respectively, intermediate values are fitted simply by interpolating between $\lambda_s^{\parallel}$ and $\lambda_s^{\perp}$, following the known shape of the magnetization derived from AMR data (see Note S4 [40]).

The values for $\lambda_s^{\parallel}$ and $\lambda_s^{\perp}$ extracted in this way are summarized in Table II, noting that the same value of $\lambda_s^{\parallel}$ is used in the reference device and the H-shaped device for Py. The absorption clearly depends on the magnetization of the FM, although this effect is much stronger in Py [Fig. 2(b)], it is also visible in Ni [Fig. 2(c)].

Although the difference between $R_{NL}^{\parallel}$ and $R_{NL}^{\perp}$ is rather small in both cases, the values for $\lambda_s^{\parallel}$ and $\lambda_s^{\perp}$ extracted from our simulations differ much more. This is due to the presence of the Sharvin resistance at the Cu/FM interfaces, which is relevant for both $\lambda_s^{\parallel}$ and $\lambda_s^{\perp}$, although much more so in the latter case. The Sharvin resistance provides a maximum conductance value of the interface. For a spin potential in the Cu channel, this acts as a resistance in series with the spin resistance of the Py injector and detector, and at short spin relaxation length in the FM absorber (below 5 nm) the Sharvin resistance contributes appreciably to the absorption. For analysis in this work, we use the value of 1.2×10^{15} fΩ^{-1} m^{-2} for all interfaces, based on *ab initio* studies of Cu/3d − FM interfaces [35,36], although a range of values can be found in the literature [32,35,36,45]. This has a significant effect on the absolute values for both values of λ_s and θ_{SHE} that we calculate. More detailed discussion can be found in Note S2 [40]. In this experiment, we observe a very small difference in values for $\lambda_s^{\parallel}$ between Py and Ni (Table II). Theoretical predictions expect a much larger value of $\lambda_s^{\parallel}$ in Ni due to its weaker exchange splitting (as high as 20 nm), as well as a somewhat larger value of $\lambda_s^{\parallel}$ in Py (5.5 nm) [32], although these predictions are all for monocrystalline materials, and in our case we have polycrystalline materials, which along with various experimental inevitabilities can be expected to lower λ_s compared with the theoretical ideal. For both materials, $\lambda_s^{\perp}$ is expected to be very small (<1 nm), due to rapid precession and dephasing of the spin current over a length scale on the order of a few interatomic distances [32,46]. Indeed we do observe a reduction of $\lambda_s^{\perp}$ compared with $\lambda_s^{\parallel}$ in both materials, although given the very small values involved for $\lambda_s^{\perp}$ it is difficult to assign an accurate value experimentally, particularly given the dependence on the interface resistance which cannot be precisely determined (Note S2 [40]).

IV. SPIN HALL EFFECT ANISOTROPY

In the same H-shaped device used for measuring absorption anisotropy, we can also measure the SHE [Fig. 1(a), black

TABLE II. Spin relaxation lengths, spin Hall angles (in units of $\hbar/e$), resistivities, and $\theta\lambda$ products at 10 K.

	ρ (Ω nm)	$\lambda_s^{\parallel}$ (nm)	$\lambda_s^{\perp}$ (nm)	$\theta_{SHE}^{\parallel}$ (%)	$\theta_{SHE}^{\perp}$ (%)	$\theta^{\parallel}\lambda^{\parallel}$ (nm)	$\theta^{\perp}\lambda^{\perp}$ (nm)
Py	313 ± 5	2.6 ± 0.2	0.9 ± 0.2	1.1 ± 0.2	4.2 ± 0.5	0.029 ± 0.007	0.038 ± 0.013
Ni	115 ± 2	3.1 ± 0.2	2.0 ± 0.2	2.3 ± 0.3	3.5 ± 0.4	0.071 ± 0.014	0.070 ± 0.015

circuit]. In this configuration, the injector magnetization, and therefore the spin polarization, is fixed along $\hat{x}$. Similarly, the direction of the spin current J_s flows almost entirely along $\hat{z}$, from the Cu channel into the FM absorber. The spin Hall current is therefore generated along $\hat{y}$, corresponding to the measured voltage. The magnitude of the effect, 2 R_{ISHE}, corresponding to the difference in the signal, $R_{ISHE} = V_{ISHE}/I_c$, where V_{ISHE} is the voltage due to the SHE, for the injector magnetized along $+\hat{x}$ and $-\hat{x}$ is shown in Fig. 3 at high field and zero field.

To perform the measurement, the injector and absorber are first magnetized along $\pm\hat{x}$ and $\pm\hat{y}$, respectively, by the application of a magnetic field along $\hat{y}$. Then the field is swept along $\hat{x}$, from 0 to $\pm$500 mT, while measuring the voltage. This process is repeated for positive and negative field sweeps, saturating the injector and detector before each sweep. In practice, and in agreement with theory, the initial orientation of the absorber ($+\hat{y}$ or $-\hat{y}$) does not affect the result, since any anisotropy with this symmetry depends on the direction but not the sign of the absorber magnetization [16]. R_{ISHE} therefore does not depend on whether the absorber is initially magnetized along $+\hat{y}$ or $-\hat{y}$, but only on $\sin^2\beta$, where β is the angle between the spin polarization and the magnetization.

Ideally, if both λ_s and θ_{SHE} were isotropic with respect to magnetization, the SHE measurement should produce a square hysteresis loop, with switching corresponding to the switching of the injector. This is because the injector switching changes the sign of the spin polarization, therefore changing the sign of V_{ISHE}, and thus R_{ISHE}. In the realistic case, we would expect to see an increase in the signal at high field as the value of λ_s increases (see Fig. 2), as well as the contribution from any change in θ_{SHE} with respect to zero field. In the case of Ni, this is indeed the case; except for jumps at low field, the signal matches what we would expect

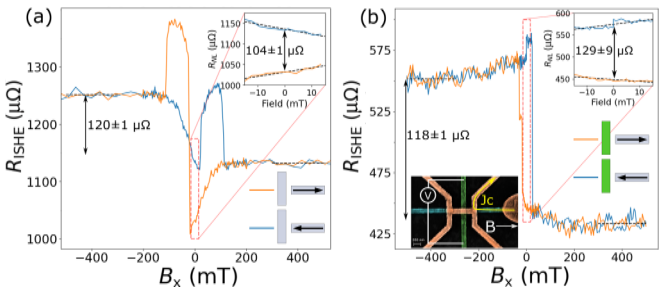

FIG. 3. SHE anisotropy measurement in (a) Py and (b) Ni, using the H-shaped device. The inset shows a false-color SEM image of the device used, indicating the applied field B_x, applied charge current J_c, and the measured voltage. The orange and blue curves correspond to the two initial magnetization states of the injector, with the top-right insets showing enlarged views at zero field. 2 R_{ISHE} at zero field and high field is annotated.

in a system where $\theta_{SHE}\lambda_s$ is approximately constant over the range of field measured.

In contrast, the data from the Py measurement are clearly quite different. There are several possible interpretations here, with artifacts possible from the planar Hall effect and anomalous Hall effect (AHE). However, these contributions would also affect Ni. Therefore, the most likely cause is the detection of spin accumulation at the interface of the FM absorber and Cu, which is measurable in Py but not in Ni. The etching of the absorber to give a clean interface with the Cu induces asymmetric domain trapping centers on both sides of the Cu channel. The magnetic texture is therefore not the same at these two sides, leading to a measurement of a nonlocal signal unrelated to spin-charge interconversion effects [11,47]. A spin accumulation measurement in Py is significantly larger than the SHE—when measuring the spin accumulation directly in the same device, we find a signal with the same symmetry as the background, but much larger (see Note S5 [40]). Detecting even a small part of this signal would be comparable to the SHE, which matches what we see here.

These spin accumulation contributions are symmetric at high magnetic field, allowing us to easily disentangle them from the antisymmetric SHE signal. At low field the spin accumulation does not contribute, meaning we directly measure just the SHE (see Note S5 [40]). The value of 2 R_{ISHE} is obtained by fitting a flat line to the R_{ISHE} values at high positive and negative field after saturation of the absorber and subtracting the values. Similarly, at low field, 2 R_{ISHE} is obtained by fitting a line to the low-field values of R_{ISHE}, thus determining the zero-field nonlocal resistance. Regardless of the behavior at intermediate fields, complicated by the presence of spin accumulation in the case of Py, the values at low and high fields are sufficient to measure the anisotropy of θ_{SHE}. In this H-shaped device we measure 2 R_{ISHE} at zero field and high field of 104 ± 1 μΩ and 120 ± 1 μΩ, respectively for Py [Fig. 3(a)], and 129 ± 9 and 118 ± 1 μΩ for Ni [Fig. 3(b)].

In this device geometry, the FM elements can be placed very close together, allowing for a large signal to be measured (Fig. 3). However, this proximity can lead to unwanted artifacts due to an appreciable fraction of the charge current reaching the absorber, although any artifacts from the AHE or magnetoresistance would be symmetric with magnetization and thus easily removed. In addition, the current is injected through the tip of the injector, and, although the magnetization is, in principle, still oriented along $\hat{x}$ at the tip, there is the potential for some noncollinear component, especially at low fields—although such effects are not seen in the reference device, Fig. 2(a).

To overcome these potential issues, we carry out the same measurement using a different geometry, the L-shaped device shown in Fig. 1(b). In this case, the FMs cannot be brought so close together, meaning a lower signal, but it does allow for current injection through the body of the injector

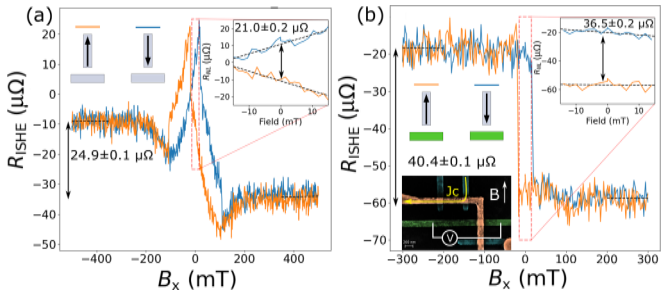

FIG. 4. SHE anisotropy measurement in (a) Py and (b) Ni using the L-shaped device. The inset shows a false-color SEM image of the devices used, indicating the applied field B_x, applied charge current J_c, and the measured voltage. The orange and blue curves correspond to the two initial magnetization states of the injector, with the top-right insets showing enlarged views at zero field. 2 R_{ISHE} at zero field and high field is annotated.

rather than the tip, as well as reduced charge current at the absorber, both of which lead to reduced potential spurious effects. Although this second geometry gives a cleaner signal, it is clearly not perfect in the case of Py, where a spin-accumulation signal is again seen [Fig. 4(a)]. For Ni, we get a square signal [Fig. 4(b)], as expected in the case of isotropic SHE in this configuration. Despite their different shapes, the two geometries share the same fundamental principle, with a perpendicularly oriented injector-absorber pair and a Cu channel allowing for nonlocal spin injection. In this L-shaped device we measure 2 R_{ISHE} at zero field and high field of 21.0 ± 0.2 and 24.9 ± 0.1 μΩ, respectively for Py [Fig. 4(a)], and 36.5 ± 0.2 and 40.4 ± 0.1 μΩ for Ni [Fig. 4(b)].

We calculated the value of θ_{SHE} for Py [Fig. 5(c)] and Ni [Fig. 5(d)] in both device geometries [Figs. 1(a) and 1(b)]. The two return very similar results for θ_{SHE}. This calculation is again performed via a 3D FEM simulation of each device, using the known value of λ_s at each field as an input parameter,

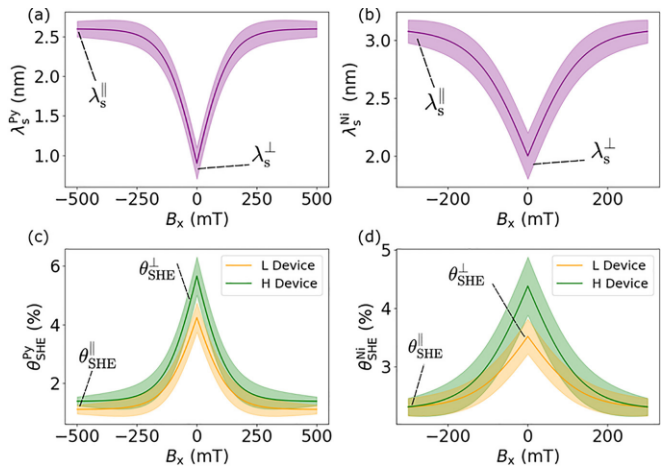

FIG. 5. Magnetic field dependence of λ_s in (a) Py and (b) Ni and θ_{SHE} in (c) Py and (d) Ni. The values of λ_s are obtained by fitting the data in Figs. 2(b) and 2(c) (H-shaped device), while θ_{SHE} is extracted from fitting the data in Figs. 3(a) and 3(b) (H-shaped device) and Figs. 4(a) and 4(b) (L-shaped device), in both cases using λ_s as an input.

TABLE III. Comparison of experimental and theoretical spin Hall conductivity values for Ni.

Reference	$\sigma_{SHE}^{\perp}$ $[\frac{\hbar}{e}]$ $(\Omega^{-1}\,\mathrm{cm}^{-1})$	$\sigma_{SHE}^{\parallel}$ $[\frac{\hbar}{e}]$ $(\Omega^{-1}\,\mathrm{cm}^{-1})$
H-shaped	3800 ± 400	2000 ± 400
L-shaped	3000 ± 400	2000 ± 300
Amin *et al.* [16]	1688	960
Salemi *et al.* [13]	1575	824

and treating θ_{SHE} as a fitting parameter. The value of θ_{SHE} is iterated until the simulated R_{ISHE} at both low and high field matches the experimental measurements, with values at intermediate fields interpolated between these two values, given the known shape of the magnetization pulling extracted from AMR measurements of the FM absorber (Note S4 [40]). The values of θ_{SHE} shown in Table II are from the L-shaped device.

We observe a large anisotropy in θ_{SHE} in both materials, although it is much larger in Py than in Ni. Interestingly, despite this very large anisotropy, the value of R_{ISHE} changes only slightly as a function of magnetization direction. This is due to the compensation of θ_{SHE} and λ_s, where R_{ISHE} $\theta_{SHE}\lambda_s$. In these materials, we appear to get an almost complete cancellation between the two quantities (i.e., $R_{ISHE}^{\parallel} \approx R_{ISHE}^{\perp}$) with λ_s being reduced greatly for spins perpendicular to the magnetization, as expected, but this being compensated by a much larger value of θ_{SHE}. Equivalently, we can say that the product, $\theta_{SHE}\lambda_s$, which is often used to express the overall efficiency of the SHE in a system is approximately constant for all values of magnetization, i.e., $\theta_{SHE}^{\parallel}\lambda_s^{\parallel} \approx \theta_{SHE}^{\perp}\lambda_s^{\perp}$ for both Py and Ni. The same result has been observed in the literature for NiCu and NiPd [11].

Comparing this to literature measurements, we see quite different results, with an experiment using magnon transport in Py observing R_{ISHE} changing by a factor of 2 between the parallel and perpendicular spin states [23]. For Ni no such experiments are available to compare with our results, however as a pure element it is comparatively better theoretically characterized than Py. In Ref. [16], the anisotropy of the SHE is decomposed into a magnetization independent SHE along with an SAHE, which arises when the spin polarization is aligned with the magnetization, which is equivalent to considering an anisotropy of the SHE with the symmetry of the SAHE as we do here. A similar calculation is carried out in Ref. [13], with the corresponding values from both theoretical works along with our experiment summarized in Table III.

Our spin Hall conductivities ($\sigma_{SHE} = \theta_{SHE}/\rho$), in both geometries are much larger than expected, by approximately a factor of 2 compared with the theory—although notably the ratio between them is comparable to the expected value. There are a number of possible explanations for this. Our values for λ_s are short in both cases. For the σ_{SHE} value extraction in Ni, we are using a λ_s in the Py injector of 2.6 nm, which is around half the theoretically expected value. A larger value of λ_s in the injector would correspond to a lower σ_{SHE} in Ni, due to increased spin injection. Indeed, if we were to use the theoretical value of λ_s in the Py from Ref. [13] of 5.5 nm, without changing the value of the Sharvin resistance we would halve our obtained σ_{SHE} in Ni. As well as this we have treated

both interfaces (Cu/Py and Cu/Ni) as being identical, but this may not be the case. Furthermore, our model ignores additional interface effects, such as spin memory loss, which would have an effect on the result but are difficult to determine accurately in a specific device [48]. Most importantly, we have seen that the precise value of the interface resistance is critical, but difficult to determine. We have used a single value from literature in our analysis, but given its large effect on λ_s and by extension the σ_{SHE}, this is a key source of uncertainty.

V. CONCLUSION

In conclusion, we have independently characterized the λ_s and θ_{SHE} of Py and Ni as a function of the relative orientation of the fixed spin current polarization and the rotating magnetization. We perform these experiments in devices with transparent and Ohmic interfaces, and spin relaxation lengths, resistivities, and polarization of all materials measured in situ.

We use two different device geometries, one based on previous experimental work (the H-shaped device) [11], which has the advantage of allowing for a larger signal due to close proximity of the injecting and absorbing element, as well as allowing the *in situ* measurement of the magnetization dependent absorption of the spin current. We repeat the spin-charge interconversion measurement in a novel geometrical configuration (L-shaped device), which allows us to remove any possible artifacts due to noncollinear magnetization at the tips of the FMs, achieving very similar results. We furthermore see a high degree of reproducibility across multiple samples using both geometries.

All the results are analyzed using 3D FEM simulations, allowing us to account for the precise geometries used and giving us an accurate description of the behavior of λ_s and θ_{SHE} in Ni and Py, which are very similar between the two geometries used. We measure a large anisotropy in λ_s for both materials [Figs. 5(a) and 5(b)], although it is more anisotropic in Py. Similarly, we see a large anisotropy in θ_{SHE} [Figs. 5(c) and 5(d)], which changes in the opposite direction to λ_s, meaning that R_{ISHE} remains relatively constant, highlighting the importance of measuring both quantities independently. Finally, we compare our values of the spin Hall conductivity in Ni to those from two theoretical works. The ratio of $\sigma^{\parallel}_{SHE}$ to $\sigma^{\perp}_{SHE}$ is similar, although our absolute values are almost twice that of the calculated ones in Ni (Table III).

ACKNOWLEDGMENTS

The authors acknowledge funding from MICIU/AEI/10.13039/501100011033 (Grant No. CEX2020-001038-M), from MICIU/AEI and ERDF/EU (Projects No. PID2021-122511OB-I00 and No. PID2021-128004NB-C21), from the European Union's Horizon 2020 research and innovation programme under the Marie Skłodowska-Curie Grant Agreement No. 955671. J.M. acknowledges funding by the Department of Education of the Basque Government under the Predoctoral Programme for the training of nondoctoral research staff (Grant No. PRE_2022_1_0297).

DATA AVAILABILITY

The data that support the findings of this article are openly available [49].

[1] J. Sinova, S. O. Valenzuela, J. Wunderlich, C. H. Back, and T. Jungwirth, Spin Hall effects, Rev. Mod. Phys. **87**, 1213 (2015).

[2] K.-W. Kim, B.-G. Park, and K.-J. Lee, Spin current and spin-orbit torque induced by ferromagnets, npj Spintron. **2**, 8 (2024).

[3] Q. Shao, P. Li, L. Liu, H. Yang, S. Fukami, A. Razavi, H. Wu, K. Wang, F. Freimuth, Y. Mokrousov, M. D. Stiles, S. Emori, A. Hoffmann, J. Akerman, K. Roy, J.-P. Wang, S.-H. Yang, K. Garello, and W. Zhang, Roadmap of spin–orbit torques, IEEE Trans. Magn. **57**, 1 (2021).

[4] S. Manipatruni, D. E. Nikonov, C.-C. Lin, T. A. Gosavi, H. Liu, B. Prasad, Y.-L. Huang, E. Bonturim, R. Ramesh, and I. A. Young, Scalable energy-efficient magnetoelectric spin–orbit logic, Nature (London) **565**, 35 (2019).

[5] J. A. C. Incorvia, T. P. Xiao, N. Zogbi, A. Naeemi, C. Adelmann, F. Catthoor, M. Tahoori, F. Casanova, M. Becherer, G. Prenat, and S. Couet, Spintronics for achieving system-level energy-efficient logic, Nat. Rev. Electr. Eng. **1**, 700 (2024).

[6] D. C. Vaz, C.-C. Lin, J. J. Plombon, W. Y. Choi, I. Groen, I. C. Arango, A. Chuvilin, L. E. Hueso, D. E. Nikonov, H. Li, P. Debashis, S. B. Clendenning, T. A. Gosavi, Y.-L. Huang, B. Prasad, R. Ramesh, A. Vecchiola, M. Bibes, K. Bouzehouane, S. Fusil *et al.*, Voltage-based magnetization switching and reading in magnetoelectric spin-orbit nanodevices, Nat. Commun. **15**, 1902 (2024).

[7] C. Qin, S. Chen, Y. Cai, F. Kandaz, and Y. Ji, Nonlocal electrical detection of spin accumulation generated by anomalous Hall effect in mesoscopic $Ni_{81}Fe_{19}$ films, Phys. Rev. B **96**, 134418 (2017).

[8] S. Iihama, T. Taniguchi, K. Yakushiji, A. Fukushima, Y. Shiota, S. Tsunegi, R. Hiramatsu, S. Yuasa, Y. Suzuki, and H. Kubota, Spin-transfer torque induced by the spin anomalous Hall effect, Nat. Electron. **1**, 120 (2018).

[9] J. D. Gibbons, D. MacNeill, R. A. Buhrman, and D. C. Ralph, Reorientable spin direction for spin current produced by the anomalous Hall effect, Phys. Rev. Appl. **9**, 064033 (2018).

[10] Y. Omori, E. Sagasta, Y. Niimi, M. Gradhand, L. E. Hueso, F. Casanova, and Y. C. Otani, Relation between spin Hall effect and anomalous Hall effect in 3*d* ferromagnetic metals, Phys. Rev. B **99**, 014403 (2019).

[11] M. Cosset-Chéneau, M. H. Fahmy, A. Kandazoglou, C. Grezes, A. Brenac, S. Teresi, P. Sgarro, P. Warin, A. Marty, V. T. Pham, J.-P. Attané, and L. Vila, Electrical measurement of the spin Hall effect isotropy in ferromagnets with strong spin-orbit interactions, Phys. Rev. B **106**, L220405 (2022).

[12] Y. Miura and K. Masuda, First-principles calculations on the spin anomalous Hall effect of ferromagnetic alloys, Phys. Rev. Mater. **5**, L101402 (2021).

[13] L. Salemi and P. M. Oppeneer, Theory of magnetic spin and orbital Hall and Nernst effects in bulk ferromagnets, Phys. Rev. B **106**, 024410 (2022).

[14] M. Seemann, D. Ködderitzsch, S. Wimmer, and H. Ebert, Symmetry-imposed shape of linear response tensors, Phys. Rev. B **92**, 155138 (2015).

[15] T. Taniguchi, J. Grollier, and M. D. Stiles, Spin-transfer torques generated by the anomalous Hall effect and anisotropic magnetoresistance, Phys. Rev. Appl. **3**, 044001 (2015).

[16] V. P. Amin, J. Li, M. D. Stiles, and P. M. Haney, Intrinsic spin currents in ferromagnets, Phys. Rev. B **99**, 220405(R) (2019).

[17] F. Zheng, M. Zhu, J. Dong, X. Li, Y. Zhou, K. Wu, and J. Zhang, Anatomy of the spin Hall effect in ferromagnetic metals, Phys. Rev. B **109**, 224401 (2024).

[18] A. Tsukahara, Y. Ando, Y. Kitamura, H. Emoto, E. Shikoh, M. P. Delmo, T. Shinjo, and M. Shiraishi, Self-induced inverse spin Hall effect in permalloy at room temperature, Phys. Rev. B **89**, 235317 (2014).

[19] J. Cramer, A. Ross, S. Jaiswal, L. Baldrati, R. Lebrun, and M. Kläui, Orientation-dependent direct and inverse spin Hall effects in $Co_{60}Fe_{20}B_{20}$, Phys. Rev. B **99**, 104414 (2019).

[20] T. Seki, S. Iihama, T. Taniguchi, and K. Takanashi, Large spin anomalous Hall effect in $L1_0$-FePt: Symmetry and magnetization switching, Phys. Rev. B **100**, 144427 (2019).

[21] Y. Koike, S. Iihama, and S. Mizukami, Composition dependence of the spin-anomalous Hall effect in a ferromagnetic Fe–Co alloy, Jpn. J. Appl. Phys. **59**, 090907 (2020).

[22] K. S. Das, J. Liu, B. J. van Wees, and I. J. Vera-Marun, Efficient injection and detection of out-of-plane spins via the anomalous spin Hall effect in permalloy nanowires, Nano Lett. **18**, 5633 (2018).

[23] K. S. Das, W. Y. Schoemaker, B. J. van Wees, and I. J. Vera-Marun, Spin injection and detection via the anomalous spin Hall effect of a ferromagnetic metal, Phys. Rev. B **96**, 220408(R) (2017).

[24] Z. Zhu, X. Zheng, G. Li, H. Bai, J. Su, Y. Zhang, and J.-W. Cai, Strong spin orientation-dependent spin current diffusion and inverse spin Hall effect in a ferromagnetic metal, NPG Asia Mater **12**, 12 (2020).

[25] T. Seki, Y.-C. Lau, S. Iihama, and K. Takanashi, Spin-orbit torque in a Ni-Fe single layer, Phys. Rev. B **104**, 094430 (2021).

[26] D. Tian, Y. Li, D. Qu, S. Y. Huang, X. Jin, and C. L. Chien, Manipulation of pure spin current in ferromagnetic metals independent of magnetization, Phys. Rev. B **94**, 020403(R) (2016).

[27] A. Yagmur, S. Sumi, H. Awano, and K. Tanabe, Large inverse spin Hall effect in Co-Tb alloys due to spin Seebeck effect, Phys. Rev. Appl. **14**, 064025 (2020).

[28] S. Varotto, M. Cosset-Chéneau, C. Grèzes, Y. Fu, P. Warin, A. Brenac, J.-F. Jacquot, S. Gambarelli, C. Rinaldi, V. Baltz, J.-P. Attané, L. Vila, and P. Noël, Independence of the inverse spin Hall effect with the magnetic phase in thin NiCu films, Phys. Rev. Lett. **125**, 267204 (2020).

[29] H. Cheng, Y. Wang, H. He, Q. Huang, and Y. Lu, Efficient and temperature-independent terahertz emission from CoFeB/NiCu heterostructures, Phys. Rev. B **105**, 155141 (2022).

[30] Z. Zhu, R. Liu, Y. Zhang, Y. Liu, Z. Yuan, and J. Cai, Crossover from positive to negative spin Hall signal in a ferromagnetic metal induced by the magnetization modulated interface effect, Adv. Phys. Res. **2**, 2370017 (2023).

[31] G. Qu, K. Nakamura, and M. Hayashi, Magnetization direction dependent spin Hall effect in 3*d* ferromagnets, Phys. Rev. B **102**, 144440 (2020).

[32] C. Petitjean, D. Luc, and X. Waintal, Unified drift-diffusion theory for transverse spin currents in spin valves, domain walls, and other textured magnets, Phys. Rev. Lett. **109**, 117204 (2012).

[33] M. Buttiker, Symmetry of electrical conduction, IBM J. Res. Dev. **32**, 317 (1988).

[34] T. Kimura, Y. Otani, T. Sato, S. Takahashi, and S. Maekawa, Room-temperature reversible spin Hall effect, Phys. Rev. Lett. **98**, 156601 (2007).

[35] A. Brataas, G. Bauer, and P. Kelly, Non-collinear magnetoelectronics, Phys. Rep. **427**, 157 (2006).

[36] M. Cosset-Chéneau, L. Vila, G. Zahnd, D. Gusakova, V. T. Pham, C. Grèzes, X. Waintal, A. Marty, H. Jaffrès, and J.-P. Attané, Measurement of the spin absorption anisotropy in lateral spin valves, Phys. Rev. Lett. **126**, 027201 (2021).

[37] F. J. Jedema, M. S. Nijboer, A. T. Filip, and B. J. van Wees, Spin injection and spin accumulation in all-metal mesoscopic spin valves, Phys. Rev. B **67**, 085319 (2003).

[38] I. I. Mazin, How to define and calculate the degree of spin polarization in ferromagnets, Phys. Rev. Lett. **83**, 1427 (1999).

[39] V. T. Pham, M. Cosset-Chéneau, A. Brenac, O. Boulle, A. Marty, J.-P. Attané, and L. Vila, Evidence of interfacial asymmetric spin scattering at ferromagnet-Pt interfaces, Phys. Rev. B **103**, L201403 (2021).

[40] See Supplemental Material at http://link.aps.org/supplemental/10.1103/dx73-2lp6 for additional measurements.

[41] P. Dular, C. Geuzaine, F. Henrotte, and W. Legros, A general environment for the treatment of discrete problems and its application to the finite element method, IEEE Trans. Magn. **34**, 3395 (1998).

[42] C. Geuzaine and J.-F. Remacle, Gmsh: A 3-D finite element mesh generator with built-in pre- and post-processing facilities, Numer. Meth Eng. **79**, 1309 (2009).

[43] E. Sagasta, Y. Omori, M. Isasa, Y. Otani, L. E. Hueso, and F. Casanova, Spin diffusion length of Permalloy using spin absorption in lateral spin valves, Appl. Phys. Lett. **111**, 082407 (2017).

[44] G. Zahnd, L. Vila, T. V. Pham, A. Marty, P. Laczkowski, W. Savero Torres, C. Beigné, C. Vergnaud, M. Jamet, and J.-P. Attané, Comparison of the use of NiFe and CoFe as electrodes for metallic lateral spin valves, Nanotechnol. **27**, 035201 (2016).

[45] G. E. W. Bauer, Y. Tserkovnyak, D. Huertas-Hernando, and A. Brataas, Universal angular magnetoresistance and spin torque in ferromagnetic/normal metal hybrids, Phys. Rev. B **67**, 094421 (2003).

[46] K. Carva and I. Turek, Spin-mixing conductances of thin magnetic films from first principles, Phys. Rev. B **76**, 104409 (2007).

[47] W. Savero Torres, V.-T. Pham, G. Zahnd, P. Laczkowski, V.-D. Nguyen, C. Beigné, L. Notin, M. Jamet, A. Marty, L. Vila, and J.-P. Attané, Using domain walls to perform non-local measurements with high spin signal amplitudes, Appl. Phys. Lett. **109**, 042405 (2016).

[48] R. Liu, K. Gupta, Z. Yuan, and P. J. Kelly, Calculating the spin memory loss at Cu|metal interfaces from first principles, Phys. Rev. B **106**, 014401 (2022).

[49] Raw data at https://zenodo.Org/records/17062686.